2020

Mechanism of Nickel Phyllosilicate Formation by Laser Ablation in Liquid

Mallory G. John
VCU

Katharine M. Tibbetts
VCU, kmtibbetts@vcu.edu

Mechanism of Nickel Phyllosilicate Formation by Laser Ablation in Liquid

Mallory G. John and Katharine Moore Tibbetts*

Department of Chemistry, Virginia Commonwealth University, Richmond, VA

E-mail: kmtibbetts@vcu.edu

Phone: +1 804 828 7515

Abstract

One-step synthesis of nickel-phyllosilicate (Ni-PS) nanocomposites was achieved using a femtosecond-reactive laser ablation in liquid (fs-RLAL) technique. Focusing intense femtosecond laser pulses onto a silicon wafer immersed in aqueous nickel nitrate generated Ni-PS with high Ni loading in excess of 20 wt.% under alkaline pH conditions. Analysis of the dissolved species in solution present after laser processing revealed that silicic acid was the key dissolved ablation product that reacted with the nickel nitrate to form the Ni-PS under alkaline conditions. When the solution was below pH 7, no silicic acid was generated from ablation, and consequently no Ni-PS was formed in the dried product. The mechanism of Ni-PS formation from fs-RLAL of a silicon wafer immersed in aqueous nickel nitrate solutions is discussed. Based on this mechanism, it is expected that the fs-RLAL method will be capable of generating a variety of metal-phyllosilicates from different metal salt precursors.

1 Introduction

Metal-phyllosilicates (M-PS) are a class of minerals comprised of layered tetrahedral and octahedral sheets of silicates and metal cations. The tetrahedral sheets contain a 'T' cation bound with four oxygen atoms, while the octahedral sheets contain a 'M' cation bound to six anions which may be O, F, Cl, or OH. Phyllosilicate structures can be composed of a 1:1 phase, made up of one repeating tetrahedral sheet and one repeating octahedral sheet, or a 2:1 phase comprised of repeating layers of one octahedral sheet sandwiched between two tetrahedral sheets.[1] The T cations are Si^{4+}, Al^{3+}, or Fe^{3+}, while the octahedral M centers are usually Mg^{2+}, Mn^{2+}, Ni^{2+}, Co^{2+}, Cu^{2+}, Zn^{2+}, etc. By choosing combinations of the T and M cations, the resulting size of the tetrahedral and octahedral centers can lead to a range of phyllosilicate morphologies include sheets and nanotubes.[1–3] Figure 1 displays the 2:1 and 1:1 phases of nickel phyllosilicate with Si^{4+} and Ni^{2+} as the T and M centers, respectively.
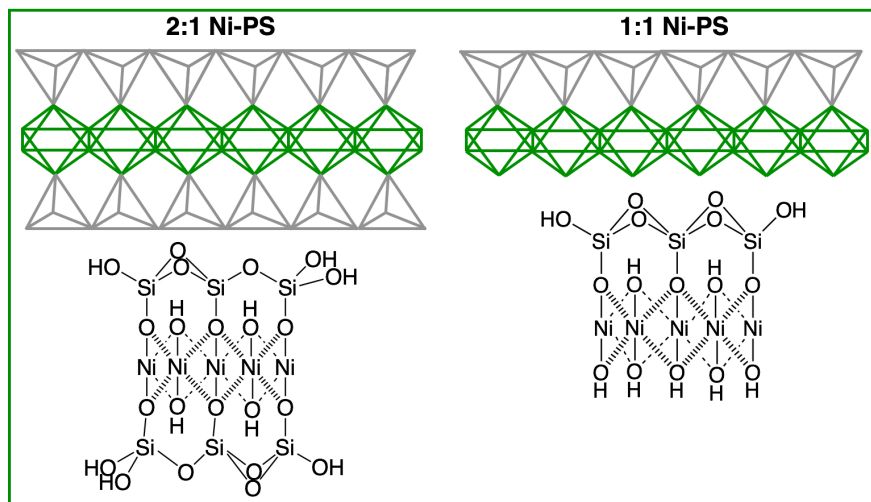
Figure 1: Nickel-phyllosilicate (Ni-PS) as 2:1 and 1:1 phases. Figure adapted from Bian *et al.*[1]

Phyllosilicate materials have gained attention recently in applications including water splitting,[4–6] supercapacitors,[7,8] lithium batteries,[9,10] drug delivery,[11,12] and catalysis.[1,13–17] The ability to substitute the T or M centers makes phyllosilicates beneficial for a variety of catalytic reactions, where the highly dispersed M^{2+} octahedral cations may be reduced in a

separate step, leading to highly dispersed ultrasmall M^0 clusters with high catalytic activity. For example, Ni^0 nanoparticles were formed over silica by H_2 reduction of a 2:1 nickel-phyllosilicate (Ni-PS) phase, which exhibited high activity and stability toward methane reforming from CO_2.[18,19] The key to the stability of this material is that the unreduced Ni^{2+} centers act as anchoring sites for the Ni^0 nanoparticles, preventing sintering. Phyllosilicates with other transition metals allow for high selectivity to catalytic reactions: copper phyllosilicates (Cu-PS) have high selectivity to methanol from CO_2 reduction as well as carbon-oxygen bond hydrogenation,[15,20,21] while cobalt-phyllosilicates (Co-PS) are active towards the Fischer-Tropsch reaction[16] and the kinetically sluggish oxygen evolution reaction (OER) half reaction of water splitting.[5]

Metal-phyllosilicates are most commonly synthesized through a variety of wet chemical approaches, including hydrothermal, deposition-precipitation, strong electrostatic adsorption, and ammonia evaporation.[1,2,22–26] In these methods, the oxidic support such as silica can be prepared from the Stöber method, from sol-gel synthesis, or a monomer silica source such as tetraethyl orthosilicate or silicic acid.[1,2,7] Subsequent introduction of the metal complex precursor to interact with the support material is conducted by heating up the slurry or solution.[1,27] The three key factors to fabricating M-PS is (a) a silica source, (b) a metal precursor, and (c) an alkaline environment (to dissolve the outer layer of silica).[1] Once formed, M-PS can be subject to a reducing step to form M^0 clusters anchored to the phyllosilicate structure through the unreduced M^{2+} sites.[13,28,29]

Recently, we reported the one-step synthesis of sub-3 nm Cu_2O clusters dispersed over copper-phyllosilicate (Cu-PS) using a laser ablation in liquid (LAL) technique in which intense laser pulses were focused on the surface of a silicon wafer immersed in an alkaline solution of $Cu(NO_3)_2$.[30] LAL comprises simple, versatile, and green synthesis strategies that employ photons to drive synthesis of a variety of nanomaterials.[31–34] For instance, LAL has been used to synthesize highly complex structured nanomaterials including Ni-Fe layered double hydroxides,[35] PtCo/CoOx nanoalloys,[36] and structurally disordered $CoFe_2O_4$/CoO

materials,[37] all of which have promising properties for catalytic applications. In the case of our femtosecond-reactive LAL (fs-RLAL), the interaction between intense ultrashort pulses and the immersed silicon wafer results in the lattice electrons absorbing the laser energy and escaping into the surrounding liquid. The resulting electron-deficient Si lattice undergoes Coulombic explosion due to the charge repulsion, ejecting out highly reactive silicon atoms and ions into the solution.[30,38–42] When the solution contains a metal salt such as $Cu(NO_3)_2$, the ejected silicon atoms and ions can react with nearby Cu^{2+} cations to form nanocomposites containing both copper and silicon.[30]

Our recent work highlighted the role that the precursor solution pH played on the product morphology when ablating a silicon wafer in $Cu(NO_3)_2$ solutions, where low pH formed Cu-core/silica shell nanoparticles while alkaline conditions formed Cu_2O/Cu-PS.[30] In this work, we investigate the reaction mechanisms underlying phyllosilicate formation by identifying the dissolved species present in solution after ablation and the roles they play in forming nickel-silica nanostructures. This was achieved by ablating a silicon wafer immersed in water and aqueous solutions of $Ni(NO_3)_2$ over a range of pH conditions. The key silicate species generated from the ablation plasma that reacted with the nickel cations to Ni-PS was silicic acid, which was only present at pH 10 and higher. The results, combined with our previous report of Cu-PS,[30] suggest that alkaline reaction conditions can be applied as a general method to prepare M-PS using fs-RLAL.

2   Methods Section

2.1   Materials

Silicon wafers (*n*-doped, (111)-oriented, single side polished, 300 μm thick, NOVA electronic materials), potassium hydroxide (KOH, Fisher), and nickel(II) nitrate ($Ni(NO_3)_2$, Fisher) were used as received. Stock and working solutions were prepared with purified water from a Millipore Ultrapure water system (resistivity is 18.2 MΩcm^{-1} at 25°C).

2.2 Sample Preparation

Working solutions were prepared directly in a 15 mL 10×40×40 mm glass cuvette from $Ni(NO_3)_2$ (50 mM) and KOH (500 mM) stock solutions. Table 1 displays the sample name and the solution composition of all samples prepared. The cuvette was equipped with a stir bar and a precut silicon wafer and irradiated for 120 min (details in Section 2.3). After irradiation was complete, the solution pH was recorded, and the sample was centrifuged for 90 min at 13,000 rpm, washed with water and repeated. The first supernatant was collected for electrospray ionization-mass spectrometry (ESI-MS) and inductively coupled plasma-optical emission spectroscopy (ICP-OES) analysis, and the powder was collected for characterization described in Section 2.4.

Table 1: Sample names and solution composition prepared in this work.

Sample Name	mM $Ni(NO_3)_2$	mM KOH	Initial pH
silica-5.9	0	0	5.9±0.05
silica-7.8	0	0.02	7.8±0.45
silica-10.3	0	0.2	10.3±0.04
silica-11.7	0	5	11.7±0.01
silica-Ni-5.9	2	0	5.9±0.01
silica-Ni-8.3	2	1	8.3±0.06
silica-Ni-10.6	2	5	10.6±0.10
silica-Ni-11.8	2	10	11.8±NA

2.3 Instrumentation

The laser ablation setup has been described in detail elsewhere.[30,41] Briefly, a Ti:sapphire-based chirped-pulse amplifier (Astrella, Coherent, Inc.) delivering 7 mJ, 30 fs pulses with bandwidth centered at 800 nm at a 1 kHz repetition rate was attenuated to 200 μJ for all ablation experiments. The silicon wafer was placed approximately 10 mm in front of the focal point of a $f = 50$ mm lens; the high numerical aperture lens ensures no filamentation occurs on the window of the cuvette or in the aqueous solution prior to interaction with

the Si wafer. The ablation spot size was 85 μm in diameter based on measurements of an ablated Si wafer with an optical microscope.

Samples were generated using 200 μJ pulses, corresponding to a laser fluence of 3.5 J cm^{-2} and an intensity of 1.2×10^{14} W cm^{-2}. The sample cuvette was placed on a miniature stir plate (Thermo Scientific) mounted to x- and y- motorized translation stages (Thorlabs). The stages were mounted on a manually controlled z-direction stage (Thorlabs), which was adjusted to focus the laser beam onto the Si wafer. The cuvette was translated in the x- and y- directions at a rate of 0.5 mm/s during the irradiation experiments to move the laser focus across the Si wafer.

2.4 Characterization

Transmission Electron Microscopy (TEM) TEM images were collected on a JEOL JEM-1230 TEM at 120 kV. Samples were prepared by drop-casting the re-dispersed powder pellet onto a carbon-coated copper grid (100 mesh, Ted Pella, Inc.) and left to dry for at least 24 hr at room temperature.

Scanning Electron Microscopy-Energy Dispersive X-ray Spectroscopy (SEM-EDX) SEM-EDX was carried out on a Hitachi FE SEM SU-70 (spatial resolution 1.0 nm) equipped with an Energy Dispersive X-ray Spectroscopy (EDX) detector. Images were obtained at 10 keV and elemental analysis was conducted at 20 keV, with ZAF standardless quantification employed for EDX measurements. Samples were prepared by depositing the dried powder pellets onto conductive carbon tape stabilized on an aluminum stage.

X-ray Diffraction (XRD) XRD was conducted on a Panalytical Empryrean Diffractometer with CuKα radiation ($\lambda = 0.15418$ nm) at 40 kV and 45 mA, with scanning angle (2θ) of $10-90°$ and a gonio focusing geometry. Samples were prepared for XRD analysis by drying the centrifuged pellet under vacuum at room temperature and collecting the dried powder.

X-ray Photoelectron Spectroscopy (XPS) XPS was conducted on a PHI VersaProbe

III Scanning XPS Microprobe with a monochromatic Al Kα X-ray source (1486.6 eV) run at 25 W and 15 KV, with a pass energy set to 112 eV for survey scans and 69 eV for high resolution spectra. A spot diameter of 100 μm was irradiated using a take off angle of 90°, and a detector was situated at an angle of 45°. Charge neutralization was achieved by employing an ion gun and a flood gun during the analysis. Samples were prepared by depositing the dried powder onto conductive carbon tape. Sample analysis was carried out using CasaXPS Software version 2.3.19PR1.0, employing Gaussian and Lorentzian convolution to fit the spectral lines, and all high resolution spectra were corrected by shifting the C1s peak at 284.8 eV.

Fourier Transform Infrared Spectroscopy (FTIR) FTIR analysis was conducted on a Nicolet iS50 FTIR spectrometer equipped with a mid- and far- IR-capable diamond ATR. Spectra were obtained using 32 scans in the range of 4000 to 400 cm^{-1} with 5 cm^{-1} resolution. Samples were prepared for FTIR analysis by drying the centrifuged pellet under vacuum at room temperature and collecting the dried powder.

Inductively Coupled Plasma-Optical Emission Spectroscopy (ICP-OES) ICP-OES was carried out on a Varian VISTA-MPX inductively coupled plasma optical emission spectrometer. Analysis of Ni content in the supernatant was achieved by centrifuging the as-prepared samples at 13,000 rpm for 90 min followed by filtering of the supernatant solution through a 0.22 μm cellulose filter, and dispersed in 6 v/v% HNO_3 in water. Calculations based on external calibration curve prepared from a 1000 ppm Ni stock (Inorganic Ventures). Calibration curve is provided in Figure S1 in the Supporting Information.

Electrospray Mass-Spectrometry (ESI-MS) ESI-MS data were run on an Orbitrap Velos from Thermo Electron in the Mass Spectrometry facility at VCU. The spray voltage was operated at 3.5 V using a flow rate of 0.7 μL/min. Data was collected using LTQ-Tune and visualized with Qual Browser (Thermo XCalibur software). Samples were prepared by filtering (0.22 μm cellulose) the supernatant (13,000 rpm for 90 min) and mixing 1:1 with acetonitrile.

3   Results and Discussion

3.1   Characterization of Dissolved Species in Solution

The prepared samples from Table 1 were centrifuged for 90 min at 13,000 rpm to ensure that all clusters and nanoparticles were separated out into the pellet, and the species present in the supernatant were only the dissolved species. ICP-OES and SEM-EDX were used to quantify the Ni content in the supernatant (as ppm) and the washed pellet (as wt.%), respectively, and the results are displayed in Figure 2, with numerical values provided in Table S1 in the Supporting Information. The silica-Ni-pH 5.9 sample had the highest concentration of Ni in the supernatant at 117.5 ppm, and the concentration of Ni in the supernatant decreased as the precursor solution pH increased up to pH 10.6. Alternatively, the wt.% Ni quantified in the dried pellets shows an inverse relationship to the Ni content quantified in the supernatant. The lowest wt.% Ni of 0.47±0.08 was in the silica-Ni-pH 5.9 pellet, and increased with solution pH up to 29.3±3.6 wt.% in the silica-Ni-pH 11.8 sample.
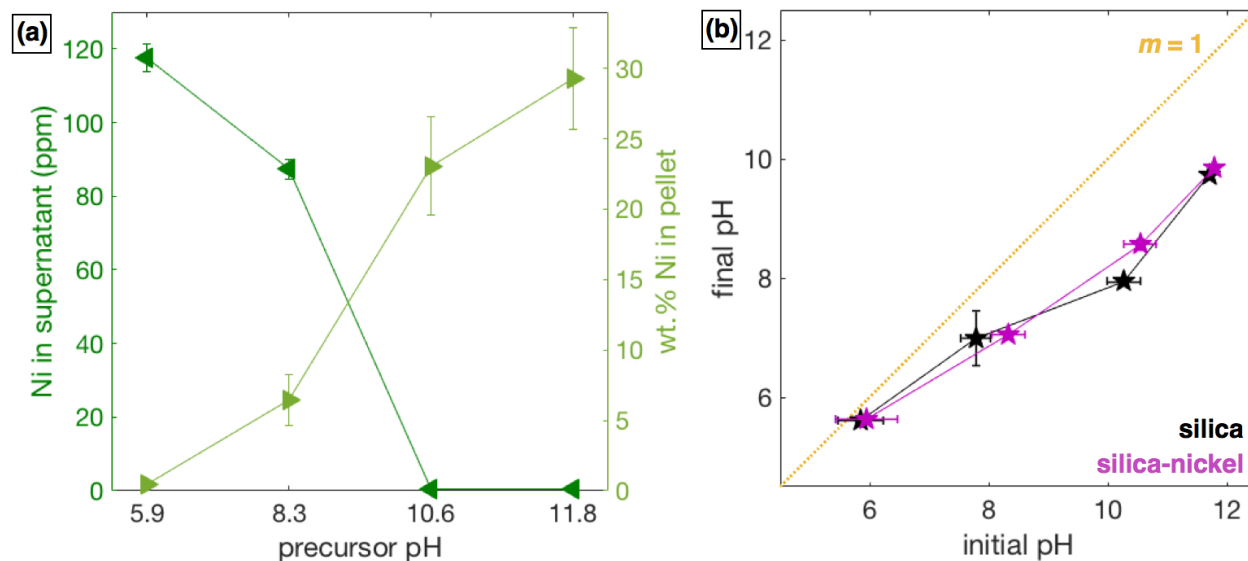

Figure 2: Nickel content in supernatant (left y-axis) and in dried pellet (right y-axis) (a); pH change of solutions before and after irradiation (b).

The precursor solution pH decreased after laser irradiation was complete, and the magnitude of this decrease was affected by the initial solution pH. Figure 2b displays the final

solution pH versus initial solution pH for all silica and silica-nickel samples, with numerical values provided in the Supporting Information, Table S1. The pH change was dependent upon the initial solution pH, and not on the added $Ni(NO_3)_2$, as the data points of the silica and silica-Ni samples are nearly overlapping. For the solutions near an initial pH of 6, nearly no pH change was observed from laser irradiation, as the data points are near the plotted line with a slope of one. As the initial pH increased, the final pH decreased, with a maximum decrease of $\sim$2 pH units for the two highest pH samples pH 10.6 and 11.8.

Because the change in solution pH upon laser irradiation was dependent upon the initial solution pH, the solution-phase silicate species generated in the low- and high-pH samples were characterized. Figure 3a and b display ESI-mass spectra of the collected supernatants of four samples at the low and high pH conditions. In Figure 3a the mass spectra of the silica-pH 5.9 and silica-Ni-pH 5.9 are compared, with peaks labeled at 76 m/z and 244 m/z. The major peak at 76 m/z in the silica-pH 5.9 sample corresponds to deprotonated metasilicate, with the structure provided in Figure 3. The metasilicate peak disappeared in the silica-Ni-pH 5.9, and a separate peak located at 244 m/z formed, corresponding to a $[(H_2O)_5NiOSi(H_2O)_2O]^-$ (Ni-O-Si) monomer species, with the structure provided in Figure 3. The presence of metasilicate upon ablation in water, along with its disappearance and subsequent formation of the Si-O-Ni monomer species upon the addition of $Ni(NO_3)_2$, suggests that the metasilicate species plays a role in forming the Si-O-Ni monomer. Previous reports on the formation of Ni-PS have identified the formation of this Ni-O-Si monomer species as being the most favorable compound formed at lower pH ranges.[43,44] When the Si wafer was ablated in high pH solutions, the metasilicate peak is present in both solutions without (silica-pH 11.7) and with $Ni(NO_3)_2$ (silica-Ni-pH 10.6) (Figure 3b; spectra are normalized to the intensity of the metasilicate peak at 76 m/z). An additional peak is present at 95 m/z, which is assigned to deprotonated silicic acid. In the silica-Ni-pH 10.6 spectrum, a relative decrease in the 95 m/z species is observed upon addition of the $Ni(NO_3)_2$ to the precursor solution. Moreover, no peak at 244 m/z is present in the silica-Ni-pH 10.6 spectrum. Other

9

peaks are assigned to a hydrated $Ni(OH)_2$ species (127 m/z) and a silicate-dimer (155 m/z). Since no major Ni-containing peaks were identified in this spectrum, it is likely that the majority of the nickel is found in the separated dried powder. It should be noted that the contribution of dissolved silicon from the glass cuvette is negligible, and the dissolved silicate species detected in the ESI-MS in Fig. 3a and b correspond to the ablated Si wafer. Calculations to determine the contribution from the glass cuvette are provided in the Supporting Information.
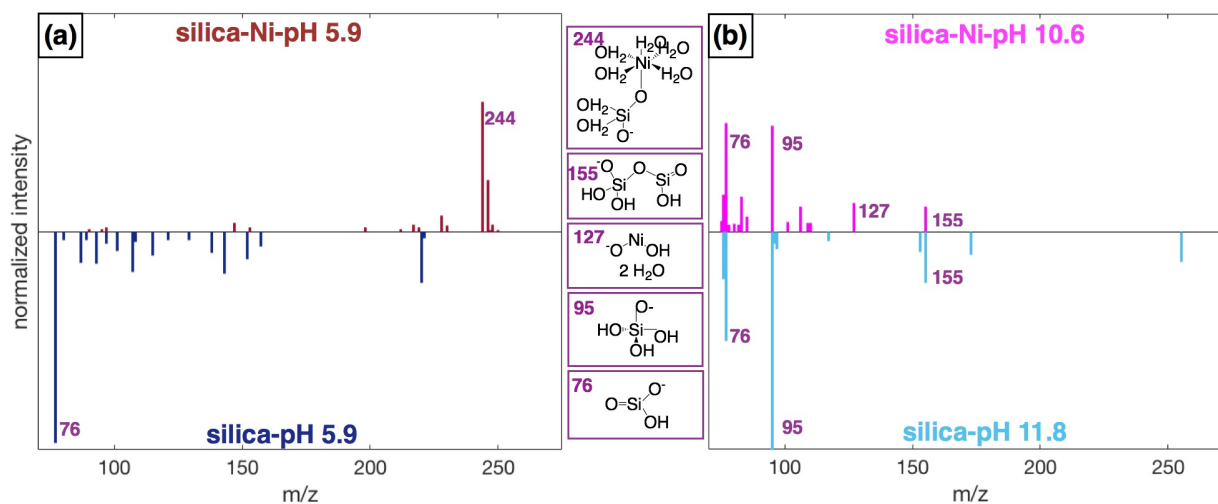

Figure 3: ESI-MS patterns for silica and silica nickel samples at different pHs.

3.2   Characterization of Solid Products

XRD patterns of the obtained solid powders in Figure 4 contain a broad peak near 25°, corresponding to amorphous silica.[45] The weakly intense peaks located at $2\theta = 28.5°$, 47°, 56°, 69°, and 76° correspond to the (111), (220), (311), (400), and (331) planes of fcc-silicon, and the cell parameter was calculated to be $a = 0.544\pm0.002$ nm, in agreement with the value of fcc-silicon (JCPDS number 27-1402).[45] These peaks are present in both the silica-and silica-Ni samples, with more intense peaks present in the silica samples prepared below pH 11.7. The fcc-silicon peaks are weakly visible in all silica-Ni samples, and decrease in intensity in the silica-Ni-10.6 and silica-Ni-11.8 samples. The silica-Ni-pH 8.3, pH 10.6, and

pH 11.8 samples also have broad peaks located at $2\theta = 34°$ and $61°$ that increase in intensity with increasing solution pH, with an additional peak near $73°$ in the silica-Ni-pH 11.8 sample. These peaks are consistent with reports of ill-crystallized nickel-phyllosilicate.[13,18,46–49] The silica-Ni-pH 5.9 pattern matches that of the XRD patterns of the nickel-free silica samples, and does not have any peaks associated with the Ni-PS phase. As the solution pH increased to 8.3, the silica-Ni-pH 8.3 pattern has both the fcc-Si peaks along with very weakly intense peaks for Ni-PS, corresponding the presence of both the fcc-Si and a small amount of Ni-PS phase in this sample. The silica-Ni-pH 10.6 and pH 11.8 samples have more intense peaks corresponding to the Ni-PS phase, and very weak peaks corresponding to fcc-Si. Thus, in this pH range, the Ni-PS is the major phase present in the powder samples.
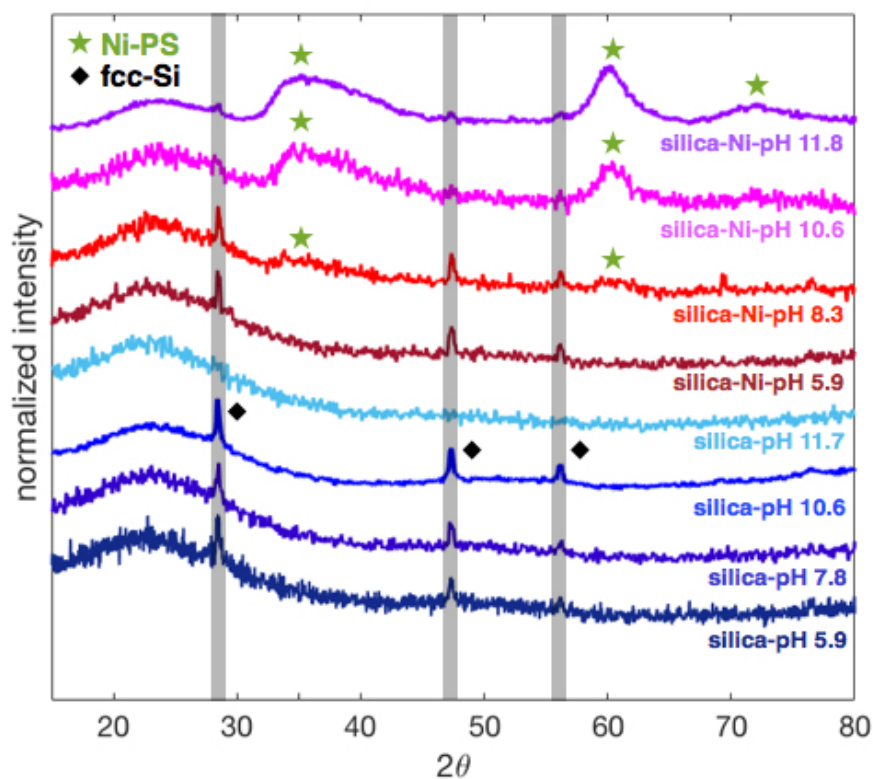

Figure 4: XRD patterns of silica and silica-nickel samples prepared from different precursor pH solutions.

TEM images of the silica-Ni samples are displayed in Figure 5 and additional TEM images are provided in Figure S2 in the Supporting Information. Representative TEM images of

the silica samples are displayed in Figure 6. The silica-Ni-pH 5.9 sample in Figure 5a has mostly amorphous silica with large spherical particles $\sim$50 nm in diameter, decorated with small $\sim$1.5 nm particles, which are visible in the inset of Figure 5a. These small particles are most likely comprised of silicon or silica, since this morphology is similar to that of the silica-pH 10.5 TEM image in Figure 6a, and due to very low nickel loading in the dried powder (Figure 2a). In the silica-Ni-pH 10.6 and pH 11.8 samples (Figure 5c–d), the morphology transformed from the mostly amorphous silica and spherical particles in Figure 5a to that of Ni-PS phase. The crinkly-like morphology of the Ni-PS visible in the insets of Figure 5c and d is consistent with the morphology of Ni-PS from previous reports.[1,13,49–51] The silica-Ni-pH 8.3 sample has a combination of amorphous silica and the Ni-PS structure, as seen in the inset of Figure 5b. The morphology of the samples from TEM corroborate the XRD patterns in Fig 4, and confirm that increased solution pH results in the formation of an ill-crystallized Ni-PS structure.

FTIR spectra are displayed in Figure 7 with inset (a) of the ν(OH) stretching region and (b) of the Si$-$O and δ(OH) bending region. The silica-pH 7.8 is displayed as a representative spectrum of the silica-only samples, as they were similar across the pH range (Supporting Information, Figure S3). The FTIR spectra of silica-pH 7.8 and silica-Ni-pH 5.9 were similar, with absorbance bands corresponding to the isolated OH groups of the silica support (3745 cm^{-1}), and the antisymmetric (1075 cm^{-1}) and symmetric (800 cm^{-1}) stretching bands of Si$-$O of the SiO$_4$ tetrahedra in silica.[18,50,52] This result suggests that the key components in the silica-Ni-pH 5.9 correspond to the silica support, with no features consistent with nickel-containing phases. The silica-Ni-pH 8.3 spectrum had peaks at 3745 cm^{-1}, 1075 cm^{-1} and 800 cm^{-1} that resembled the silica-7.8 and silica-Ni-pH 5.9 spectra. An additional absorbance at 670 cm^{-1} was identified that was not observed in the two other spectra, and corresponds to the δ(OH) bending mode of the 1:1 Ni-PS structure.[18,50,52] The silica-Ni-pH 10.6 sample lacks the 3745 cm^{-1} feature, exhibits a decrease in absorbance at 800 cm^{-1}, and has a shift in the 1075 cm^{-1} peak to 1020 cm^{-1}. These spectral features are consistent
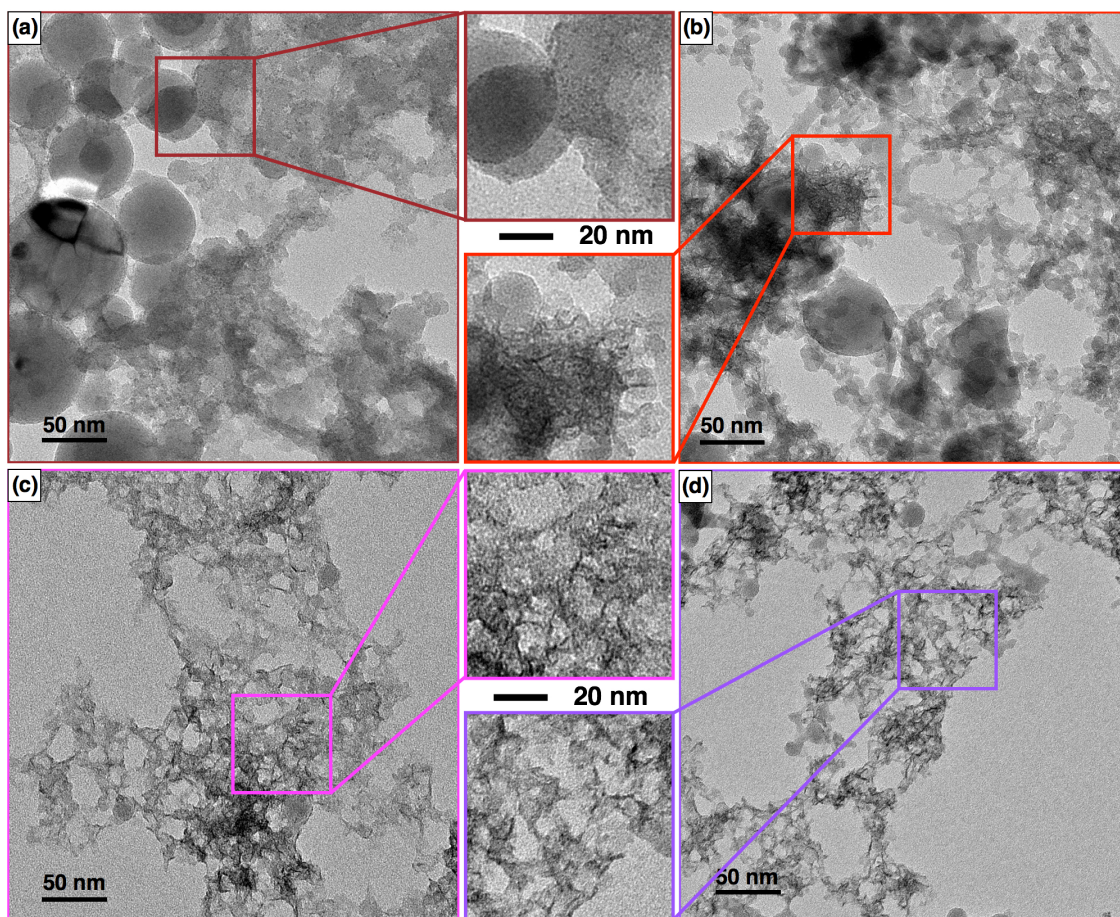
Figure 5: TEM images of silica-Ni samples at pH 5.9 (a), 8.3 (b), 10.6 (c), and 11.8 (d).
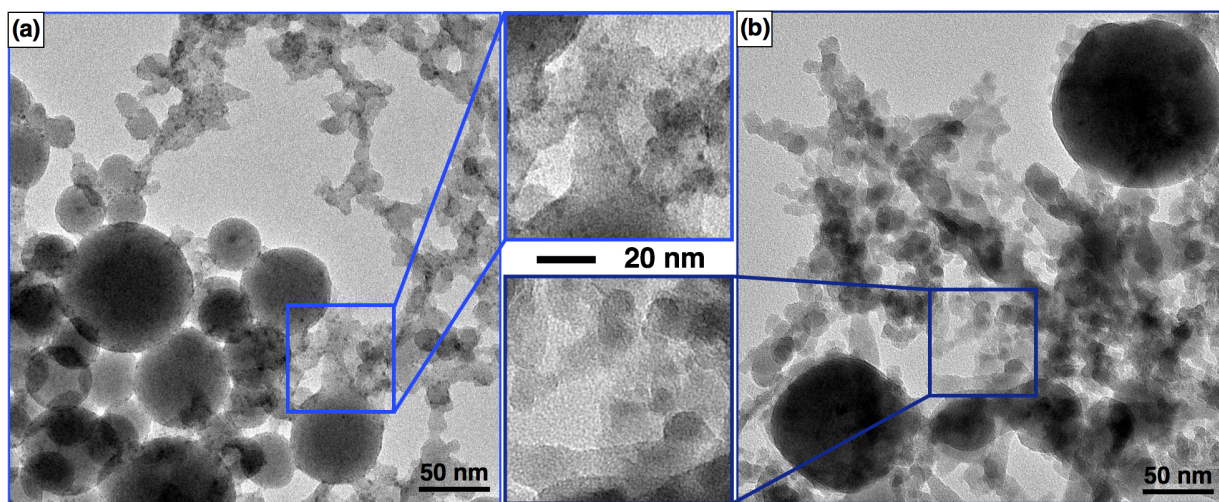

Figure 6: TEM images of silica NPs generated at pH 10.5 (a) and in water at pH 5.9 (b).

with the disappearance of the isolated OH groups of silica and the formation of Si–O–Ni bonds of Ni-PS. The observed 1020 cm^{-1} frequency corresponds to the 2:1 Ni-PS phase; the 1:1 Ni-PS phase would be expected at 1005 cm^{-1}.[52,53] The silica-Ni-pH 10.6 sample also exhibits a new broad feature around 650 cm^{-1}. This feature could arise from the δ(OH) bending mode of a 1:1 Ni-PS phase at 670 cm^{-1}, an ill-crystallized α-Ni(OH)$_2$ structure at 640 cm $^{-1}$, or both.[35,49,52] In the silica-Ni-pH 11.8 spectrum, this feature has an even more asymmetric absorbance in the 640 cm^{-1} range than near 670 cm^{-1}, which suggests a greater contribution from Ni(OH)$_2$. The silica-Ni-pH 11.8 also contains a small but sharp peak at 3645 cm^{-1} (inset (a)), corresponding to the ν(OH) stretching vibration in either the 1:1 Ni-PS phase or in β-Ni(OH)$_2$.[35,52]
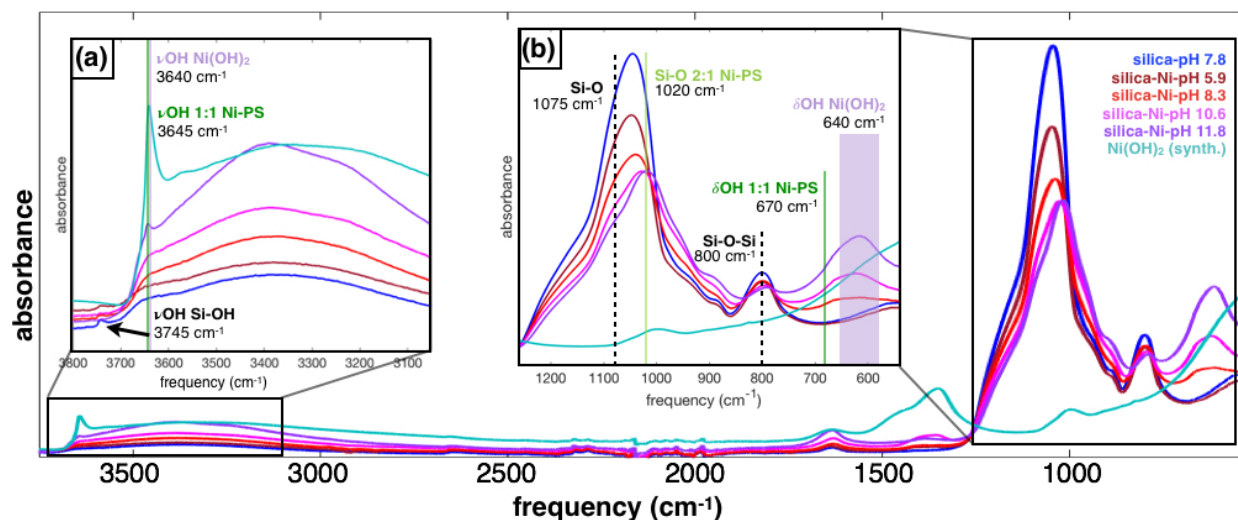

Figure 7: FTIR spectra of silica and silica-nickel samples prepared from different precursor solution pH.

To determine the origin of the sharp peak at 3645 cm^{-1} in the silica-Ni-pH 11.8 spectrum, the precursor Ni(NO$_3$)$_2$ solution was centrifuged and dried (13,000 rpm, 90 min) and the FTIR spectrum of the collected powder is displayed in Figure 7 (Ni(OH)$_2$ (synth.)). This spectrum has a sharp peak at 3640 cm^{-1}, confirming that this feature in the silica-Ni-pH 11.8 spectrum is due to unreacted, precipitated Ni(OH)$_2$ from the precursor. Additionally, the absorbance in inset (b) of Figure 7 of the Ni(OH)$_2$ (synth.) spectrum is near 520 cm^{-1},

consistent with the $\delta(OH)$ bending mode of the β-Ni(OH)$_2$ phase.[35,52] Thus, the absorbance band of the silica-Ni-pH 8.3, pH 10.6, and pH 11.8 samples near 640 cm^{-1} likely arise from the Ni(OH)$_2$ phase. The precursor solution pH increase from the silica-Ni-pH 8.3 to the silica-Ni-pH 11.8 samples presents shifts in absorbance intensity and frequency that are consistent with the formation of Ni-PS and Ni(OH)$_2$. The silica-Ni-pH 11.8 sample also contains some unreacted, β-Ni(OH)$_2$, as evidenced by the spectrum of its dried precursor.

The Ni2p$_{3/2}$ atomic orbital spectra obtained with XPS from silica-Ni-pH 8.3, 10.6, and 11.8 are displayed in Figure 8. No Ni was detected in the silica-Ni-pH 5.9 sample. In all three samples the surface Ni atoms possess a Ni^{2+} charge state due to lack of features in the range of Ni^0 (852.7 eV).[54] The silica-Ni-pH 10.6 and 11.8 spectra are fit to two peaks assigned to the 1:1 and 2:1 Ni-PS phases, and the silica-Ni-pH 8.3 spectrum was fit with one peak at 855.3 eV assigned to the 1:1 Ni-PS phase.[35,50,54] Because the binding energy of Ni(OH)$_2$ at 855$-$856 eV overlaps that of the 1:1 Ni-PS phase (885.5 eV), it is difficult to definitively assign the peaks in this binding energy range. The similar binding energy of Ni(OH)$_2$ to that of the Ni in 1:1 Ni-PS is due to the octahedrally coordinated Ni^{2+} to both Ni-O-Si and Ni-OH bonds in the 1:1 structure as seen in Figure 1. While it is difficult to definitively assign surface Ni species to Ni(OH)$_2$ or Ni-PS with XPS, the the spectra of the silica-Ni-pH 10.6 and 11.8 samples are consistent with Ni-PS phases observed with XRD, TEM, and FTIR.

3.3   Discussion

Analysis of solution phase silicate species generated from laser ablation and characterization of the nickel-containing products revealed that silicic acid is the key species generated under alkaline conditions (above pH 10) that reacts with nickel cations in solution to form Ni-PS. When no KOH was added to the nickel nitrate precursor solution, no silicic acid was generated, and a Si-O-Ni monomer was the major product that remained in solution. The generation of the silicic acid at high solution pH conditions drove the decrease in solution
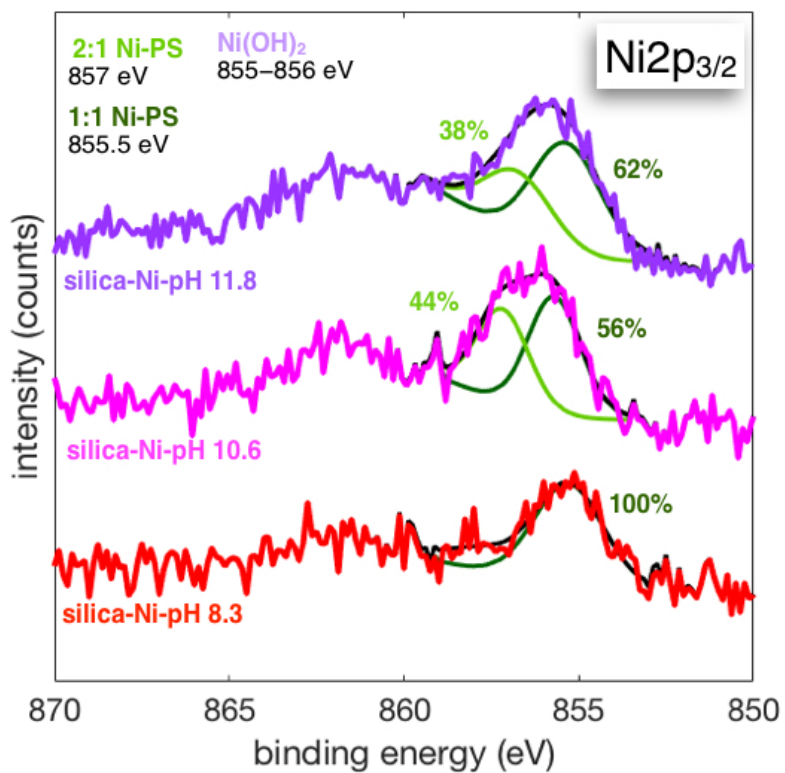
Figure 8: High resolution XP spectra of $Ni2p_{3/2}$ atomic orbital for silica-Ni samples prepared at different pH solutions.

pH after laser irradiation, independent of the addition of nickel nitrate to the precursor. The magnitude of solution pH decrease after irradiation corresponds to the relative amount of silicic acid generated. Solutions of pH ~6 had no drop in pH after irradiation, and no peak at 95 m/z in the ESI-MS. The samples with initial pH ~10.6 and ~11.8 decreased to ~8.6 and ~9.9, respectively, while the intermediate pH ~8 dropped only one pH unit, suggesting that a smaller amount of silicic acid was generated in this pH range. Analysis of the dried silica-Ni powders confirmed that silicic acid is the major species driving the formation of Ni-PS. The silica-Ni-pH 5.9 sample had nearly identical FTIR or XRD features as the silica-only samples, while the silica-Ni-pH 10.6 sample exhibited distinct features consistent with Ni-PS. The silica-Ni-pH 8.3 sample had a mixture of XRD, FTIR, and TEM features to that of the silica-Ni-pH 5.9 and the silica-Ni-pH 10.6 samples, consistent with the availability of less silicic acid for Ni-PS formation. Figure 9 displays a summary of the proposed reaction process to form the solution-phase compounds and solid-phase products in this investigation.
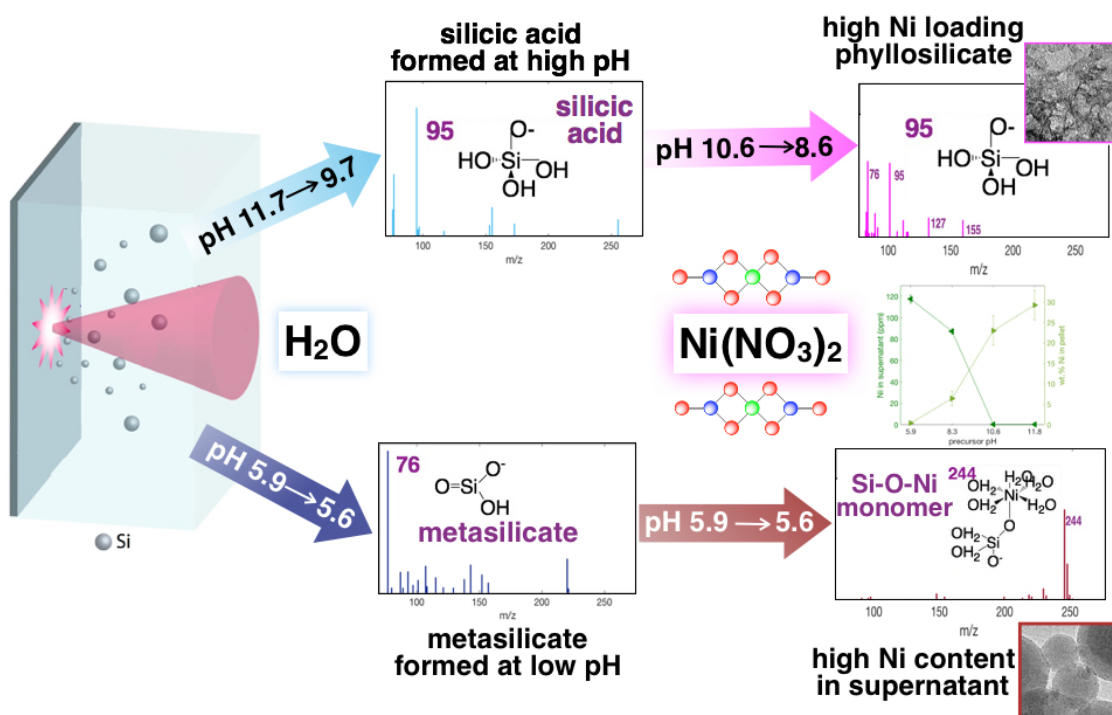

Figure 9: Proposed reaction mechanisms based on dissolved species generated from silicon wafer ablation in various solutions.

It should be noted that the formation of nickel hydroxide ($Ni(OH)_2$) is common at high solution pH, and precipitates above pH 9.[52] Because the silica-Ni-pH 11.8 sample dropped to a pH of 9.9 after laser irradiation, any unreacted nickel in the solution was likely incorporated in the dried pellet as precipitated $Ni(OH)_2$. FTIR analysis of the dried silica-Ni-pH 11.8 precursor confirmed the presence of β-$Ni(OH)_2$ in the irradiated silica-Ni-pH 11.8 sample. Thus, the 29.3 wt.% Ni in the dried powder represents both the Ni-PS and some unreacted β-$Ni(OH)_2$. In contrast, the 23.1 wt.% Ni in the silica-Ni-pH 10.6 sample represents the Ni-PS phase, since the final solution pH of 8.6 is below the precipitation point of $Ni(OH)_2$, as evidenced by the 127 m/z peak corresponding to hydrated $Ni(OH)_2$ in the supernatant via ESI-MS.

The majority of synthesis approaches to Ni-PS include deposition-precipitation (D-P) and hydrothermal treatments, where the silica source (silicic acid, sodium silicate, fumed silica) is mixed with the nickel precursor ($NiCl_2$, $Ni(NO_3)_2$), and the solution pH was controlled by addition of urea. Investigations on the effect of the Si/Ni ratio, specific surface area (SSA) of the silica precursor, and D-P reaction time have lead to the observations that the Si/Ni ratio, the solution pH, and SSA of the silica source affected the relative yields of $Ni(OH)_2$ as compared to 1:1 or 2:1 Ni-PS structures.[1,43,44,52,53] Low SSA silica formed $Ni(OH)_2$ over silica in one report[52] and $Ni(OH)_2$ with 1:1 Ni-PS in a separate report.[43] High SSA silica and solution pH formed 2:1 Ni-PS, as long as the pH was below the $Ni(OH)_2$ precipitation threshold.[43,52,53]

In this work, silicic acid was generated directly *in situ* through the laser ablation process, wherein ejected silicon atoms form silicic acid upon interaction with solution. The silicic acid monomer was only observed in ESI-MS in the high pH samples of the silica-pH 11.7 and silica-Ni-pH 10.6 samples. In the two samples prepared at pH $\sim$6, a metasilicate species was identified in ESI-MS, which was attributed to the $[(H_2O)_5NiOSi(H_2O)_2O]^-$ monomer formation. Previous reports on the formation mechanism of Ni-PS structures have suggested that silicic acid or its deprotonated $(OH)_3SiO^-$ form is responsible for the formation of this

$[(H_2O)_5NiOSi(H_2O)_2O]^-$ monomer, which was suggested as an intermediate species in Ni-PS formation.[1,43,44,52,53] Our data do not support the above hypothesis, but suggest that the metasilicate species is responsible for forming the $[(H_2O)_5NiOSi(H_2O)_2O]^-$ monomer, which is not a Ni-PS intermediate. The silicic acid formed at high pH instead drives the Ni-PS formation.

The ablation reaction conditions used to form Ni-PS in this work were similar to those used in our recent publication reporting ultrasmall Cu_2O nanoparticles dispersed over copper-phyllosilicate (Cu-PS).[30] In the latter work, Cu-PS formation was attributed to the silica clusters becoming deprotonated and attracting nearby $Cu_2(OH)_2^{2+}$ complexes due to strong electrostatic attraction.[30] However, the findings from this investigation identify the silicic acid as the primary driver of metal-phyllosilicate formation. The formation of both Cu-PS in our recent publication and the Ni-PS in this work demonstrate a general method of metal-phyllosilicate synthesis using a laser ablation in liquid technique. The key to successfully preparing metal phyllosilicates requires that the solution have a high enough pH to induce silica dissolution resulting in silicic acid generated that may interact with the divalent metal cations. Because both copper nitrate and nickel nitrate formed Cu-PS and Ni-PS under similar experimental conditions, the specific metal salts used do not appear to play as large of a role in the metal-phyllosilicate formation as the ablated silicate species do. These results suggest that the laser ablation in liquid technique can become a versatile route to a variety of metal phyllosilicate materials with very high metal loadings. These materials are expected to provide exceptional thermal stability and high activity for catalytic applications.

4 Conclusion

The synthesis of nickel-phyllosilicate with 23 wt.% Ni was achieved using the fs-RLAL method by ablating a silicon wafer immersed in nickel nitrate solutions under alkaline conditions. Analysis of the supernatants of irradiated solutions revealed that silicic acid was the

key species driving the nickel-phyllosilicate formation when the solution pH was above 10. The generation of silicic acid led to a decrease of solution pH by two pH units after laser irradiation. In contrast, for irradiated solutions of nickel nitrate and water at ∼pH 6, the solution pH did not change after irradiation, no silicic acid was detected in the supernatants, and nearly no nickel was detected in the dried powder. Instead, a metasilicate species as the major product in when the silicon wafer was ablated in water, while a Si-O-Ni monomer was the major species detected when nickel nitrate was added to the solution. The results from this work and from our recent report[30] identify a general mechanism of metal-phyllosilicate synthesis using laser ablation liquid under alkaline conditions. The metal cation complex does not appear to play a large role in metal-PS formation, but rather the solution pH drives the metal-PS formation due to the silicic acid generated from the ablation process. This synthesis method may be applied to other divalent metal cations to fabricate metal-phyllosilicates that may be used for catalytic applications.

Supporting Information Available

The Supporting Information (SI) is available free of charge on the ACS Publication website. Included in the SI is a table of nickel content in the supernatant and dried pellet for the silica-Ni samples, a calibration curve for ICP-OES quantification for Ni in the supernatants, calculations to determine the dissolved silicon contribution from the glass cuvette, Si concentration (ppm) in the supernatants of the silica-Ni samples, additional TEM images for the silica-Ni samples, and FTIR spectra of the silica-containing samples. This material is available free of charge via the Internet at `http://pubs.acs.org/`.

Acknowledgement

References

(1) Bian, Z.; Kawi, S. Preparation, Characterization and Catalytic Application of Phyllosilicate: A Review. *Catal. Today* **2020**, *339*, 3 – 23.

(2) McDonald, A.; Scott, B.; Villemure, G. Hydrothermal Preparation of Nanotubular Particles of a 1:1 Nickel Phyllosilicate. *Micropor. Mesopor. Mater.* **2009**, *120*, 263 – 266.

(3) Alvarez-Ramírez, F.; Toledo-Antonio, J. A.; Angeles-Chavez, C.; Guerrero-Abreo, J. H.; López-Salinas, E. Complete Structural Characterization of $Ni_3Si_2O_5(OH)_4$ Nanotubes: Theoretical and Experimental Comparison. *J. Phys. Chem. C* **2011**, *115*, 11442–11446.

(4) Ghiat, I.; Boudjemaa, A.; Saadi, A.; Bachari, K.; Coville, N. J. Efficient Hydrogen Generation over a Novel Ni Phyllosilicate Photocatalyst. *J. Photochem. Photobiol. A: Chem.* **2019**, *382*, 111952.

(5) Kim, J. S.; Park, I.; Jeong, E.-S.; Jin, K.; Seong, W. M.; Yoon, G.; Kim, H.; Kim, B.; Nam, K. T.; Kang, K. Amorphous Cobalt Phyllosilicate with Layered Crystalline Motifs as Water Oxidation Catalyst. *Adv. Mater.* **2017**, *29*, 1606893.

(6) Qiu, C.; Jiang, J.; Ai, L. When Layered Nickel–Cobalt Silicate Hydroxide Nanosheets Meet Carbon Nanotubes: A Synergetic Coaxial Nanocable Structure for Enhanced Electrocatalytic Water Oxidation. *ACS Appl. Mater. & Interf.* **2016**, *8*, 945–951.

(7) Zhao, J.; Zheng, M.; Run, Z.; Xia, J.; Sun, M.; Pang, H. 1D $Co_{2.18}Ni_{0.82}Si_2O_5(OH)_4$

Architectures Assembled by Ultrathin Nanoflakes for High-Performance Flexible Solid-State Asymmetric Supercapacitors. *J. Power Sources* **2015**, *285*, 385 – 392.

(8) Zhao, J.; Zhang, Y.; Wang, T.; Li, P.; Wei, C.; Pang, H. Reed Leaves as a Sustainable Silica Source for 3D Mesoporous Nickel (Cobalt) Silicate Architectures Assembled into Ultrathin Nanoflakes for High-Performance Supercapacitors. *Adv. Mater. Interfaces* **2015**, *2*, 1400377.

(9) Yang, Y.; Liang, Q.; Li, J.; Zhuang, Y.; He, Y.; Bai, B.; Wang, X. $Ni_3Si_2O_5(OH)_4$ Multi-Walled Nanotubes with Tunable Magnetic Properties and their Application as Anode Materials for Lithium Batteries. *Nano Res.* **2011**, *4*, 882–890.

(10) Zhang, X.-Q.; Li, W.-C.; He, B.; Yan, D.; Xu, S.; Cao, Y.; Lu, A.-H. Ultrathin Phyllosilicate Nanosheets as Anode Materials with Superior Rate Performance for Lithium Ion Batteries. *J. Mater. Chem. A* **2018**, *6*, 1397–1402.

(11) Ganguly, S.; Das, N. C. Synthesis of a Novel pH Responsive Phyllosilicate Loaded Polymeric Hydrogel Based on Poly(acrylic acid-co-N-vinylpyrrolidone) and Polyethylene Glycol for Drug Delivery: Modelling and Kinetics Study for the Sustained Release of an Antibiotic Drug. *RSC Adv.* **2015**, *5*, 18312–18327.

(12) Viseras, C.; Aguzzi, C.; Cerezo, P.; Bedmar, M. C. Biopolymer–Clay Nanocomposites for Controlled Drug Delivery. *Mater. Sci. Tech.* **2008**, *24*, 1020–1026.

(13) Yang, M.; Jin, P.; Fan, Y.; Huang, C.; Zhang, N.; Weng, W.; Chen, M.; Wan, H. Ammonia-Assisted Synthesis Towards a Phyllosilicate-Derived Highly-Dispersed and Long-Lived Ni/SiO_2 Catalyst. *Catal. Sci. Technol.* **2015**, *5*, 5095–5099.

(14) Zhang, Q.; Wang, M.; Zhang, T.; Wang, Y.; Tang, X.; Ning, P. A Stable Ni/SBA-15 Catalyst Prepared by the Ammonia Evaporation Method for Dry Reforming of Methane. *RSC Adv.* **2015**, *5*, 94016–94024.

(15) Zhao, Y.; Zhang, Y.; Wang, Y.; Zhang, J.; Xu, Y.; Wang, S.; Ma, X. Structure evolution of mesoporous silica supported copper catalyst for dimethyl oxalate hydrogenation. *Appl. Catal. A: Gen.* **2017**, *539*, 59 – 69.

(16) Cai, J.; Jiang, F.; Liu, X. Exploring Pretreatment Effects in Co/SiO_2 Fischer-Tropsch Catalysts: Different Oxidizing Gases Applied to Oxidation-Reduction Process. *Appl. Catal. B: Environ.* **2017**, *210*, 1 – 13.

(17) Park, J. C.; Kang, S. W.; Kim, J.-C.; Kwon, J. I.; Jang, S.; Rhim, G. B.; Kim, M.; Chun, D. H.; Lee, H.-T.; Jung, H.; Song, H.; *et al.*, Synthesis of Co/SiO_2 Hybrid Nanocatalyst via Twisted $Co_3Si_2O_5(OH)_4$ Nanosheets for High-Temperature Fischer–Tropsch Reaction. *Nano Res.* **2017**, *10*, 1044–1055.

(18) Sivaiah, M.; Petit, S.; Barrault, J.; Batiot-Dupeyrat, C.; Valange, S. CO_2 Reforming of CH_4 over Ni-Containing Phyllosilicates as Catalyst Precursors. *Catal. Today* **2010**, *157*, 397 – 403.

(19) Sivaiah, M.; Petit, S.; Beaufort, M.; Eyidi, D.; Barrault, J.; Batiot-Dupeyrat, C.; Valange, S. Nickel Based Catalysts Derived from Hydrothermally Synthesized 1:1 and 2:1 Phyllosilicates as Precursors for Carbon Dioxide Reforming of Methane. *Micropor. Mesopor. Mater.* **2011**, *140*, 69 – 80.

(20) Li, F.; Wang, L.; Han, X.; Cao, Y.; He, P.; Li, H. Selective Hydrogenation of Ethylene Carbonate to Methanol and Ethylene Glycol over Cu/SiO_2 Catalysts Prepared by Ammonia Evaporation Method. *Int. J. Hydrogen Energ.* **2017**, *42*, 2144 – 2156.

(21) Gong, X.; Wang, M.; Fang, H.; Qian, X.; Ye, L.; Duan, X.; Yuan, Y. Copper Nanoparticles Socketed In Situ into Copper Phyllosilicate Nanotubes with Enhanced Performance for Chemoselective Hydrogenation of Esters. *Chem. Commun.* **2017**, *53*, 6933–6936.

(22) Ding, J.; Popa, T.; Tang, J.; Gasem, K. A.; Fan, M.; Zhong, Q. Highly Selective and

Stable Cu/SiO$_2$ Catalysts Prepared with a Green Method for Hydrogenation of Diethyl Oxalate into Ethylene Glycol. *Appl. Catal. B: Environ.* **2017**, *209*, 530 – 542.

(23) Eskandari, S.; Tate, G.; Leaphart, N. R.; Regalbuto, J. R. Nanoparticle Synthesis via Electrostatic Adsorption Using Incipient Wetness Impregnation. *ACS Catal.* **2018**, *8*, 10383–10391.

(24) Chen, L.-F.; Guo, P.-J.; Qiao, M.-H.; Yan, S.-R.; Li, H.-X.; Shen, W.; Xu, H.-L.; Fan, K.-N. Cu/SiO$_2$ Catalysts Prepared by the Ammonia-Evaporation Method: Texture, Structure, and Catalytic Performance in Hydrogenation of Dimethyl Oxalate to Ethylene Glycol. *J. Catal.* **2008**, *257*, 172 – 180.

(25) Cao, L.; Raciti, D.; Li, C.; Livi, K. J. T.; Rottmann, P. F.; Hemker, K. J.; Mueller, T.; Wang, C. Mechanistic Insights for Low-Overpotential Electroreduction of CO$_2$ to CO on Copper Nanowires. *ACS Catalysis* **2017**, *7*, 8578–8587.

(26) Jiao, L.; Regalbuto, J. R. The Synthesis of Highly Dispersed Noble and Base Metals on Silica via Strong Electrostatic Adsorption: I. Amorphous Silica. *J. Catal.* **2008**, *260*, 329 – 341.

(27) Zhang, C.; Yue, H.; Huang, Z.; Li, S.; Wu, G.; Ma, X.; Gong, J. Hydrogen Production via Steam Reforming of Ethanol on Phyllosilicate-Derived Ni/SiO$_2$: Enhanced Metal–Support Interaction and Catalytic Stability. *ACS Sustain. Chem. Eng.* **2013**, *1*, 161–173.

(28) Ashok, J.; Kathiraser, Y.; Ang, M. L.; Kawi, S. Ni and/or Ni–Cu Alloys Supported Over SiO$_2$ Catalysts Synthesized via Phyllosilicate Structures for Steam Reforming of Biomass Tar Reaction. *Catal. Sci. Technol.* **2015**, *5*, 4398–4409.

(29) Bian, Z.; Kawi, S. Highly Carbon-Resistant Ni–Co/SiO$_2$ Catalysts Derived from Phyllosilicates for Dry Reforming of Methane. *J. CO2 Util.* **2017**, *18*, 345 – 352.

(30) John, M. G.; Tibbetts, K. M. Controlling the Morphology of Copper-Silica Nanocomposites from Laser Ablation in Liquid. *Appl. Surf. Sci.* **2020**, *510*, 145037.

(31) Semaltianos, N. G. Nanoparticles by Laser Ablation. *Crit. Rev. Solid State Mater. Sci.* **2010**, *35*, 105–124.

(32) Zhang, D.; Gökce, B.; Barcikowski, S. Laser Synthesis and Processing of Colloids: Fundamentals and Applications. *Chem. Rev.* **2017**, *117*, 3990–4103.

(33) Reichenberger, S.; Marzun, G.; Muhler, M.; Barcikowski, S. Perspective of Surfactant-Free Colloidal Nanoparticles in Heterogeneous Catalysis. *Chem. Cat. Chem.* **2019**, *11*, 4489–4518.

(34) Amendola, V.; Amans, D.; Ishikawa, Y.; Koshizaki, N.; Scirè, S.; Compagnini, G.; Reichenberger, S.; Barcikowski, S. Room-Temperature Laser Synthesis in Liquid of Oxide, Metal-Oxide Core-Shells and Doped Oxide Nanoparticles. *Chem. Eur. J.* **2020**, DOI: 10.1002/chem.202000686.

(35) Hunter, B. M.; Blakemore, J. D.; Deimund, M.; Gray, H. B.; Winkler, J. R.; Müller, A. M. Highly Active Mixed-Metal Nanosheet Water Oxidation Catalysts Made by Pulsed-Laser Ablation in Liquids. *J. Am. Chem. Soc.* **2014**, *136*, 13118–13121.

(36) Hu, S.; Goenaga, G.; Melton, C.; Zawodzinski, T. A.; Mukherjee, D. PtCo/CoOx Nanocomposites: Bifunctional Electrocatalysts for Oxygen Reduction and Evolution Reactions Synthesized via Tandem Laser Ablation Synthesis in Solution-Galvanic Replacement Reactions. *Appl. Catal. B: Environ.* **2016**, *182*, 286 – 296.

(37) Waag, F.; Gökce, B.; Kalapu, C.; Bendt, G.; Salamon, S.; Landers, J.; Hagemann, U.; Heidelmann, M.; Schulz, S.; Wende, H.; *et al.*, Adjusting the Catalytic Properties of Cobalt Ferrite Nanoparticles by Pulsed Laser Fragmentation in Water with Defined Energy Dose. *Sci. Rep.* **2017**, *7*, 13161.

(38) Gamaly, E. G.; Rode, A. V.; Luther-Davies, B.; Tikhonchuk, V. T. Ablation of Solids by Femtosecond Lasers: Ablation Mechanism and Ablation Thresholds for Metals and Dielectrics. *Phys. Plasmas* **2002**, *9*, 949–957.

(39) Gamaly, E. *Femtosecond Laser-Matter Interaction: Theory, Experiments and Applications*; Pan Stanford Publishing: Singapore, 2011.

(40) Sobhan, M. A.; Withford, M. J.; Goldys, E. M. Enhanced Stability of Gold Colloids Produced by Femtosecond Laser Synthesis in Aqueous Solution of CTAB. *Langmuir* **2010**, *26*, 3156–3159.

(41) John, M. G.; Tibbetts, K. M. One-step Femtosecond Laser Ablation Synthesis of Sub-3 nm Gold Nanoparticles Stabilized by Silica. *Appl. Surf. Sci.* **2019**, *475*, 1048 – 1057.

(42) Wang, C.; Huo, H.; Johnson, M.; Shen, M.; Mazur, E. The Thresholds of Surface Nano-/Micro-Morphology Modifications with Femtosecond Laser Pulse Irradiations. *Nanotech.* **2010**, *21*, 075304.

(43) Burattin, P.; Che, M.; Louis, C. Molecular Approach to the Mechanism of Deposition-Precipitation of the Ni(II) Phase on Silica. *J. Phys. Chem. B* **1998**, *102*, 2722–2732.

(44) Mizutani, T.; Fukushima, Y.; Okada, A.; Kamigaito, O. Synthesis of Nickel and Magnesium Phyllosilicates with 1:1 and 2:1 Layer Structures. *Bull. Chem. Soc. Jpn.* **1990**, *63*, 2094–2098.

(45) Shao, M.; Hu, H.; Ban, H.; Li, M.; Gao, H. Fabrication of Large-Scale, Layer-Deposited, Low Oxygen-Content and Uniform Silicon Nanowires. *J. Cryst. Growth* **2007**, *303*, 391 – 394.

(46) Ye, R.-P.; Gong, W.; Sun, Z.; Sheng, Q.; Shi, X.; Wang, T.; Yao, Y.; Razink, J. J.; Lin, L.; Zhou, Z.; *et al.*, Enhanced Stability of Ni/SiO$_2$ Catalyst for CO$_2$ Metha-

nation: Derived from Nickel Phyllosilicate with Strong Metal-Support Interactions. *Energy* **2019**, *188*, 116059.

(47) Burattin, P.; Che, M.; Louis, C. Characterization of the Ni(II) Phase Formed on Silica Upon Deposition-Precipitation. *J. Phys. Chem. C* **1997**, *101*, 7060–7074.

(48) Krasilin, A. A.; Nevedomsky, V. N.; Gusarov, V. V. Comparative Energy Modeling of Multiwalled $Mg_3Si_2O_5(OH)_4$ and $Ni_3Si_2O_5(OH)_4$ Nanoscroll Growth. *J. Phys. Chem. C* **2017**, *121*, 12495–12502.

(49) Kong, X.; Zhu, Y.; Zheng, H.; Li, X.; Zhu, Y.; Li, Y.-W. Ni Nanoparticles Inlaid Nickel Phyllosilicate as a Metal–Acid Bifunctional Catalyst for Low-Temperature Hydrogenolysis Reactions. *ACS Catal.* **2015**, *5*, 5914–5920.

(50) Lehmann, T.; Wolff, T.; Hamel, C.; Veit, P.; Garke, B.; Seidel-Morgenstern, A. Physico-Chemical Characterization of Ni/MCM-41 Synthesized by a Template Ion Exchange Approach. *Micropor. Mesopor. Mater.* **2012**, *151*, 113 – 125.

(51) Wang, Z.-Q.; Xu, Z.-N.; Peng, S.-Y.; Zhang, M.-J.; Lu, G.; Chen, Q.-S.; Chen, Y.; Guo, G.-C. High-Performance and Long-Lived Cu/SiO_2 Nanocatalyst for CO_2 Hydrogenation. *ACS Catal.* **2015**, *5*, 4255–4259.

(52) Kermarec, M.; Carriat, J. Y.; Burattin, P.; Che, M.; Decarreau, A. FTIR Identification of the Supported Phases Produced in the Preparation of Silica-Supported Nickel Catalysts. *J. Phys. Chem.* **1994**, *98*, 12008–12017.

(53) Chen, B.-H.; Chao, Z.-S.; He, H.; Huang, C.; Liu, Y.-J.; Yi, W.-J.; Wei, X.-L.; An, J.-F. Towards a Full Understanding of the Nature of Ni(II) Species and Hydroxyl Groups over Highly Siliceous HZSM-5 Zeolite Supported Nickel Catalysts Prepared by a Deposition–Precipitation Method. *Dalton Trans.* **2016**, *45*, 2720–2739.

(54) Nesbitt, H. W.; Legrand, D.; Bancroft, G. M. Interpretation of Ni2p XPS Spectra of Ni Conductors and Ni Insulators. *Phys. Chem. Miner.* **2000**, *27*, 357–366.

TOC Graphic

silicic acid

pH 11.7→9.7

H₂O

pH 5.9→5.6

metasilicate

Si

Ni(NO₃)₂

pH 10.6→8.6

pH 5.9 → 5.6

high Ni loading
Ni-phyllosilicate

20 nm

low Ni loading